

APPENDIX A. EXAMPLE: CALIBRATION OF A CRYOGENIC BLACKBODY

Raju U. Datla, Eric L. Shirley, Albert C. Parr

National Institute of Standards and Technology, Gaithersburg, Maryland, USA

A.1 Introduction

There are different scenarios for using radiometrically calibrated sensors in space. One scenario is that the sensor is launched into space or stationed in space to identify and track an object such as a missile in its midcourse travel in space. The sensor would see the distant object as a point source against the characteristic space background of a few Kelvin. Radiometric calibration of such a sensor in the laboratory has to be done for the flux levels expected in space using a well-known source such as a point-source blackbody in an environment simulating space. The calibration of such a point-source blackbody in order to use it as a standard for sensor calibration is discussed in this Appendix taking the data from Datla et al. [1] as an example.

A.2 Calibration of a Cryogenic Point-Source Blackbody

In Section 1.5.1, the basic principles for the point-source blackbody calibration have been discussed. Figure 1.7 illustrates the basic experimental setup with an absolute cryogenic radiometer (ACR) as the detector. The ACR directly measures the radiant power irradiating its precision aperture in watts. The geometric data of the calibration setup for a blackbody calibration at National Institute of Standards and Technology (NIST) is given in Table A.1 with associated uncertainties. The values given in Column 2 are for the cryogenic temperatures of operation and are deduced from ambient measurements using known temperature dependence of expansion of materials.

Table A.2 shows the blackbody measurements [1]. Column 1 shows the nominal setting of the blackbody temperature. Column 2 shows the mean values of measurements of the platinum resistance thermometer mounted on the blackbody core. Column 3 shows the standard deviation for 1 s repetitions at each setting. The measured value of the radiant power Φ at the ACR aperture is shown in Column 4. Each of the measurements was

TABLE A.1. Geometric Data for Cryogenic Blackbody Calibration Setup

Quantity	Value	Uncertainty in measurement (1σ) (%)
1. Blackbody aperture radius (r_1) at 20 K	0.3244 mm	$\delta r_1/r_1 = 0.2$
2. Radius (r_2) of the ACR aperture at 2.2 K	1.4971 cm	$\delta r_2/r_2 = 0.003$
3. Distance between the apertures (R) at 20 K	30.77 cm	$\delta R/R = 0.136$

repeated at 1.5 s intervals for 3 min. Three repeated measurements taken at different times to assess the reproducibility are shown. These measured values need to be corrected for diffraction effects in order to use geometrical optics and deduce the blackbody radiance temperature T . The diffraction effects are discussed in Section A.2.1, and the corrections are given in Table A.3. The values of radiant power corrected for diffraction, Φ_0 , are shown in Column 5 of Table A.2. The radiance temperature is then deduced by using the Stefan–Boltzmann formula,

$$T = \left(\frac{\Phi_0}{F_{12}A_1\sigma} \right)^{1/4} \quad (\text{A.1})$$

The value of the Stefan–Boltzmann constant is $\sigma = 5.6704 \times 10^{-8} \text{ W/m}^2/\text{K}^4$. The configuration factor F_{12} is evaluated by using the data in Table A.1 and Eq. (1.13) in Section 1.3.3. The deduced radiance temperatures of the blackbody are shown in Table A.2, Column 6. Column 7 shows the standard deviations of the deduced temperatures, s_{ij} , using Eq. (A.1) for each of the 120 measurements of radiant flux at each setting.

A.2.1 Diffraction Correction

As discussed in Chapter 9, the radiant power Φ from the blackbody incident at the ACR aperture is not solely determined according to geometrical optics because of diffraction effects at both limiting and non-limiting apertures in the beam path shown in Figure A.1. Therefore, diffraction losses at each one of the apertures in the beam path are estimated by using the procedures described in Chapter 9. The measured radiant power values are corrected for diffraction effects at each aperture in the beam path. Table A.3 gives the calculated correction factors, $(\Phi_0 - \Phi)/\Phi = \Delta\Phi/\Phi$, as a percentage of the measured radiant power for various temperatures.

Figure A.1 illustrates the geometry of the optical setup. Items shown are not to relative scale. From left to right, they are (1) the blackbody cavity and

TABLE A.2. Blackbody Measurements, before and after Corrections, and Uncertainties

(1) Nominal blackbody temp. (K)	(2) Blackbody sensor temp. (K)	(3) Std. dev. (K)	(4) Measured power (nW)	(5) Diffraction- corrected power (nW)	(6) Radiance temp. (K)	(7) Std. dev. s_{ij} (K)	(8) Weight w_{ij}
200	199.874	0.002	72.0	73.29	201.713	1.420	0.4959
	199.897	0.005	71.9	73.19	201.643	3.500	0.0816
	199.947	0.002	70.6	71.87	200.725	2.130	0.2204
225	224.780	0.003	113.5	115.32	225.910	2.990	0.1119
	224.728	0.003	113.4	115.21	225.861	1.384	0.5221
	224.823	0.004	113.0	114.81	225.661	1.975	0.2564
250	249.662	0.004	171.3	173.70	250.272	2.100	0.2268
	249.639	0.007	172.6	175.02	250.750	1.166	0.7355
	249.733	0.005	172.2	174.61	250.600	1.865	0.2875
275	274.685	0.003	252.6	255.88	275.724	1.102	0.8234
	274.644	0.006	252.2	255.48	275.620	1.319	0.5748
	274.719	0.006	252.8	256.09	275.779	1.101	0.8249
300	299.531	0.007	358.4	362.70	300.851	0.715	1.9561
	299.521	0.003	357.3	361.59	300.620	1.135	0.7763
	299.588	0.005	358.4	362.70	300.851	0.887	1.2710
325	324.412	0.005	497.6	503.07	326.491	0.830	1.4516
	324.457	0.005	492.8	498.22	325.701	0.603	2.7502
	324.446	0.003	493.4	498.83	325.800	1.076	0.8637
350	349.306	0.003	665.8	672.46	351.059	0.644	2.4112
	349.337	0.008	663.7	670.34	350.782	0.997	1.0060
	349.445	0.006	664.8	671.45	350.927	0.869	1.3242
375	374.047	0.005	882.2	891.02	376.648	0.660	2.2957
	374.069	0.003	875.7	884.46	375.953	0.816	1.5018
	374.171	0.006	877.0	885.77	376.092	1.467	0.4647
400	399.026	0.005	1138.0	1148.24	401.303	0.872	1.3151
	399.056	0.004	1134.6	1144.81	401.003	1.266	0.6239
	399.131	0.003	1138.8	1149.10	401.373	1.217	0.6752

its opening, (2) the defining aperture (diameter-0.6488 mm) on the variable aperture disk, (3) the baffle on the front of the blackbody housing, (4) an isothermal plate, (5) the first ACR baffle, and (6) the precision ACR limiting aperture. The blackbody cavity opening and its distance from the 0.6488-mm-diameter aperture define the filling angle of the 0.6488 mm aperture. This filling angle is small enough that blackbody radiation underfills the baffle on the front of the blackbody housing, which has minimal diffraction effects. Similarly, the first ACR baffle defines the field of view seen by the

TABLE A.3. Calculated Diffraction Correction ($\Delta\Phi/\Phi$) Given as a Percentage of the Measured Radiant Power (Φ). Systematic Uncertainty (type B) in the Correction Due to All Approximations in the Calculations is $\pm 10\%$ of $\Delta\Phi/\Phi$

(1) Nominal blackbody temp. (K)	(2) Diffraction correction, $\Delta\Phi/\Phi$ (%)	(3) Uncertainty (1σ) (%)
200	1.8	± 0.18
225	1.6	± 0.16
250	1.4	± 0.14
275	1.3	± 0.13
300	1.2	± 0.12
325	1.1	± 0.11
350	1.0	± 0.10
375	1.0	± 0.10
400	0.9	± 0.09

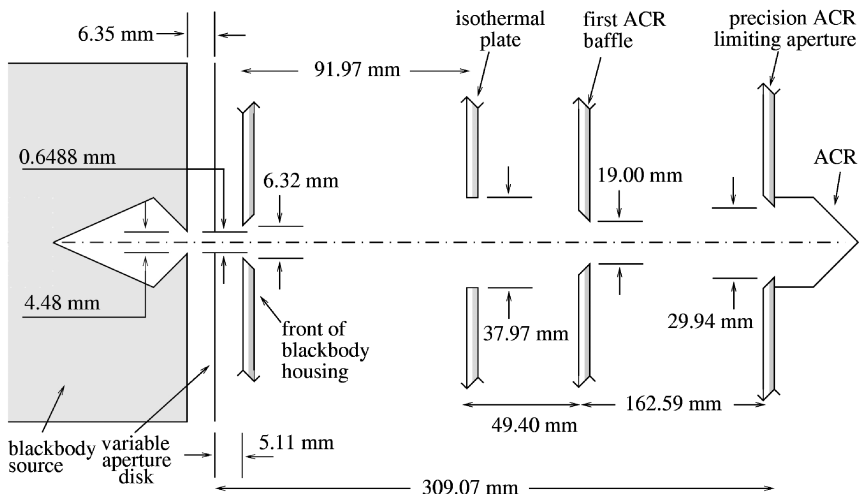


FIG. A.1. Optical setup for blackbody calibration.

ACR, so that the isothermal plate also has minimal diffraction effects. This is fortunate because the perimeter of the latter is not a knife edge and it is hard to characterize related diffraction effects.

There are two main diffraction effects: a loss because of the 0.6488 mm defining aperture, and a gain because of the first ACR baffle. One can estimate the loss by treating the blackbody cavity opening as an extended source, treating the precision ACR limiting aperture as a detector, and

considering diffraction effects of the 0.6488 mm defining aperture. One can estimate the gain by treating the 0.6488 mm defining aperture as a source, the precision ACR limiting aperture as a detector, and considering diffraction effects of the first ACR baffle. There are many options for treating diffraction effects, as discussed in greater detail in Chapter 9. For completeness, a few points are also mentioned here. Section 9.4.3.1 discusses how to estimate the loss and gain separately. Section 9.4.3.2 discusses how these effects may be approximately combined as described below.

Diffraction at the 0.6488 mm aperture affects the spectral power $\Phi_{\lambda}^{(1)}(\lambda)$ reaching the detector in the first hypothetical three-element setup by multiplying it by $F_1(\lambda) = \Phi_{\lambda}^{(1)}(\lambda)/\Phi_{\lambda}^{(1,0)}(\lambda)$, where $\Phi_{\lambda}^{(1,0)}(\lambda)$ is the corresponding ideal spectral power. Diffraction at the first ACR baffle affects the spectral power $\Phi_{\lambda}^{(2)}(\lambda)$ reaching the detector in the second hypothetical three-element setup by multiplying it by $F_2(\lambda) = \Phi_{\lambda}^{(2)}(\lambda)/\Phi_{\lambda}^{(2,0)}(\lambda)$, where $\Phi_{\lambda}^{(2,0)}(\lambda)$ is the corresponding ideal spectral power. The spectral power $\Phi_{\lambda}(\lambda)$ in the actual set is multiplied by a spectral diffraction factor $F(\lambda) = \Phi_{\lambda}(\lambda)/\Phi_{\lambda}^0(\lambda)$, where $\Phi_{\lambda}^0(\lambda)$ is the corresponding ideal spectral power. In this case one has $F(\lambda) \approx F_1(\lambda)F_2(\lambda)$.

The more detailed methods discussed in Section 9.5.1.2 can treat diffraction effects more precisely and account for the series of optics through which radiation passes. In the context of such a calculation, one can explicitly show that the diffraction effects of the front of the blackbody housing and isothermal plate are inconsequential. The dashed curve in Figure A.2 in-

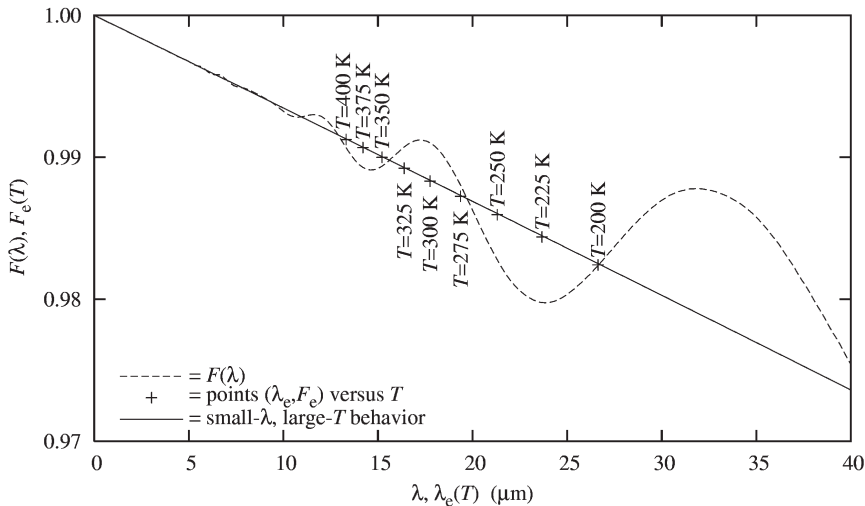


FIG. A.2. Diffraction effects on spectral and total power in setup in Figure A.1.

dicates $F(\lambda)$. For example, there is about a 2.5% loss of spectral power at 40 μm because of diffraction. In this and many other cases, the methods of Sections 9.4.3.1, 9.4.3.2, 9.5.1.2 give very similar results. Diffraction effects on spectral power increase in size with wavelength, being almost linear at the shortest wavelengths, but with an increasingly larger oscillatory part at longer wavelengths.

For diffraction effects on total power Φ , one may introduce an overall effective diffraction factor $F_e = \Phi/\Phi_0 = \int_0^\infty d\lambda F(\lambda) \Phi_\lambda^0(\lambda) / \int_0^\infty d\lambda \Phi_\lambda^0(\lambda)$, where Φ_0 is the corresponding ideal total power, and one has $\Delta\Phi/\Phi = 1/F_e - 1$. The crosses in Figure A.2 indicate calculated values of F_e at various temperatures. When plotting these results in such a way, the abscissa is λ_e , the effective wavelength (see Section 9.5.2.1). For a Planck source, one has

$$\lambda_e = \frac{\int_0^\infty d\lambda \lambda \Phi_\lambda^0(\lambda)}{\int_0^\infty d\lambda \Phi_\lambda^0(\lambda)} = \frac{\int_0^\infty d\lambda \lambda^{-4} \{\exp[c_2/(\lambda T)] - 1\}^{-1}}{\int_0^\infty d\lambda \lambda^{-5} \{\exp[c_2/(\lambda T)] - 1\}^{-1}} \approx \frac{5326.473 \text{ μm K}}{T}.$$

Here λ_e is in μm, T is in K, and $c_2 \approx 0.01437752(25)$ m K is the second radiation constant. (In the intermediate steps, there are also other, canceling factors in the numerator and denominator that are discussed in Chapter 1.) The solid curve in Figure A.2 extrapolates the small- λ behavior of $F(\lambda)$ (see Section 9.4.2.1) or large- T behavior of F_e (see Section 9.5.2.2) to larger λ or λ_e . The solid curve approximates the crosses very accurately, and much better than would using $F(\lambda_e)$, which would follow the dashed curve. This is a frequent trait of broadband radiation that is discussed further in Section 9.5.2.1.

A.2.2 Radiance Temperature and Calibration Uncertainty

The final radiance temperatures for the calibration are obtained by the least-squares analysis of temperatures, T_{ij} ($i = 1, \dots, n$; $j = 1, \dots, 3$), deduced from Eq. (A.1) as a function of blackbody sensor settings, X_{ij} ($i = 1, \dots, n$; $j = 1, \dots, 3$). In order to evaluate a confidence band for the variability of the calibration curve, the following statistical procedure is followed. The calibration equation is assumed to follow the model

$$T_{ij} = a_0 + a_1 X_{ij} + a_2 X_{ij}^2 + a_3 X_{ij}^3 + \dots + a_k X_{ij}^k + \varepsilon_{ij} \quad (\text{A.2})$$

where a_0, \dots, a_k are to be estimated, and ε_{ij} , the random errors associated with the measurements T_{ij} , are assumed to be independent with heterogeneous variances σ_{ij}^2 . The σ_{ij} are estimated from the standard deviation s_{ij} from approximately 120 data points for each temperature setting. Weighted least-squares analysis [2] accounts for the heterogeneity of variances where the weights, w_{ij} , are calculated from the empirical variances, s_{ij}^2 , by

$$w_{ij} = 1/s_{ij}^2 \quad (\text{A.3})$$

and are given in Table A.2, Column 8. The standard deviations associated with T_{ij} are an order of magnitude larger than the standard deviations associated with X_{ij} data. Therefore, random uncertainties associated with the measurements X_{ij} are negligible for the purpose of least-squares analysis.

The degree k for the polynomial in Eq. (A.2) is determined by a goodness-of-fit test that compares the agreement among three runs with the overall fit to the data. The lowest degree polynomial which satisfies the goodness-of-fit criterion is taken as the calibration curve. The least-squares analysis model is not an expression of physical law and it is only a statistical approximation for prediction of unknown values based on the given data. Therefore, one should use a minimal number of fitting coefficients [3]. For a blackbody, the ideal T versus X fit would be linear with unit slope and zero bias, i.e. the contact temperature sensor readout would be the same as the radiant temperature measured. If a linear fit is not satisfactory, one should critically examine why it fails before accepting a higher-order polynomial. A deviation from a linear fit in the current experiment would suggest that sources of radiation other than the blackbody are contributing to the radiometer output. These could be objects such as aperture holders and baffles that heat up radiatively due to the blackbody radiation and are in the field of view of the radiometer. In such an event, eliminating these possibilities by proper heat sinking and repeating the experiment would be appropriate. A slope other than unity also suggests a possible, uncorrected error in the presumed blackbody aperture radius r_1 , radiometer aperture radius r_2 , or distance between the apertures, R , or stray light from the blackbody. However, these errors can sometimes be calibrated out in the linear fit and the resulting expression.

In any case, for a polynomial fit, given a future blackbody sensor setting, X_h , its calibrated radiance temperature value is given by

$$T_h = a'_0 + a'_1 X_h + a'_2 X_h^2 + a'_3 X_h^3 + \cdots + a'_k X_h^k \quad (\text{A.4})$$

where a'_0, \dots, a'_k are least-squares estimates from calibration data. The random component of uncertainty U_r associated with the predicted value is computed as

$$U_r = [(k+1)F(95, k+1, n-k-1)]^{1/2} s(T_h) \quad (\text{A.5})$$

The constant $F(95, k+1, n-k-1)$ is the upper 95 percentile of Snedecor's F -distribution with $k+1$ degrees of freedom in the numerator and $n-k-1$ degrees of freedom in the denominator, and $s(T_h)$ is the standard deviation of the predicted value, T_h . This uncertainty, based on the Working-Hoe-

telling confidence bands for the calibration curve, is valid for all future applications of the calibration curve as long as the model holds. The details of the statistical analysis can be found in References [4, 5]. Fitting is also discussed in Section 6.16.

In the least-squares analysis, the temperature values measured by the platinum resistance thermometer (PRT) sensor (Table A.2, Column 2) are used for the independent variable, X . Analysis shows that a linear function ($k = 1$) is sufficient for describing the data. The equation,

$$T_h = a'_0 + a'_1 X_h \quad (\text{A.6})$$

gives the predicted radiance temperature T_h for a blackbody temperature X_h measured by the PRT sensor, as shown in Columns 3 and 2 of Table A.4, respectively. Column 1 shows the nominal temperature controller setting. The estimated coefficients and associated standard deviations are

$$\begin{aligned} a'_0 &= -0.89, & s(a'_0) &= 0.26 \\ a'_1 &= +1.007, & s(a'_1) &= 0.0008 \end{aligned} \quad (\text{A.7})$$

Covariance between the fitted parameters is taken into account when propagating the uncertainties.

The percentage uncertainty in the deduced radiance temperature $\delta T/T$ is given by Eq. (A.1) and the theory of uncertainty propagation [6]. An approximation on a Taylor series expression gives the relationship between the variables as

$$\frac{\delta T}{T} \approx \frac{\delta \Phi}{4\Phi} + \frac{\delta r_1}{2r_1} + \frac{\delta r_2}{2r_2} + \frac{\delta R}{2R} \quad (\text{A.8})$$

The first term on the right-hand side of Eq. (A.8) shows the relationship to

TABLE A.4. Predicted Radiance Temperatures (temp.) and Uncertainties (unc.) for Blackbody Nominal Temperature Settings

(1) Nominal blackbody temp. (K)	(2) PRT sensor output (K)	(3) Predicted radiance temp. (K)	(4) 1σ random unc., $s(T_h)$ (K)	(5) ACR char. (K)	(6) Diffraction calculation unc. (K)	(7) Geometry measurement unc. (K)	(8) Total b (K)	(9) Expanded unc. U (K)
200	199.92	200.48	0.11	0.06	0.09	0.24	0.26	0.75 (0.4%)
225	224.78	225.52	0.09	0.07	0.09	0.27	0.29	0.80 (0.4%)
250	249.68	250.60	0.07	0.08	0.09	0.30	0.32	0.87 (0.3%)
275	274.68	275.78	0.06	0.09	0.09	0.33	0.35	0.94 (0.3%)
300	299.55	300.83	0.04	0.09	0.09	0.36	0.38	1.01 (0.3%)
325	324.45	325.91	0.04	0.10	0.09	0.39	0.41	1.09 (0.3%)
350	349.36	351.01	0.04	0.11	0.09	0.42	0.44	1.17 (0.3%)
375	374.12	375.94	0.06	0.11	0.09	0.45	0.47	1.25 (0.3%)
400	399.07	401.07	0.07	0.12	0.09	0.48	0.50	1.33 (0.3%)

the contribution from the uncertainty in the radiant power which has both type A and B components. The type A component of uncertainty is essentially folded into the least-squares analysis through weights given by Eq. (A.3) to each of the deduced temperature readings. So $s(T_h)$, obtained from the least-squares analysis which includes the covariance of the fitting parameters, gives the type A component of uncertainty and is shown in Column 4 of Table A.4. The type B component of the uncertainty due to systematic effects in the first term of Eq. (A.8) are listed separately in Columns 5 and 6. Column 5 gives the uncertainty in the power, $\delta\Phi/(4\Phi)$, due to the characterization of ACR as an absolute detector based on the principle of electrical substitution explained in detail in Chapter 2, and Column 6 gives the uncertainty in diffraction calculations. The other type B components are obtained by propagating the geometry uncertainties given in Table A.1 using the last three terms in Eq. (A.8). Their combined contribution to the temperature measurement uncertainty is shown in Column 7. Column 8 shows the total type B component, b , which is the square root of the sum of squares of all type B components given in Columns 5–7. The expanded uncertainty, U , as shown in Column 9, is obtained by expanding Eq. (A.5) as follows (see [1], p. 85):

$$U = [(k + 1)F(95, k + 1, n - k - 1)]^{1/2}[s^2(T_h) + b^2]^{1/2} \quad (\text{A.9})$$

The multiplying factor in Eq. (A.9) for $n = 27$, $k = 1$ for the data is 2.6. The value shown in parenthesis in Column 9 is the expanded uncertainty given in Kelvin and as a percentage of the measured temperature in parenthesis. Figure A.3 shows the 95% confidence band for the difference between the calibrated temperature and the PRT temperature. The points represent the same with measured radiance temperatures. The expanded uncertainty given in Table A.4 is within 0.4%. However, it can be seen from Figure A.3 that this model fits well in the middle range of temperatures and not at the extreme low and high temperatures.

The statistical procedure that leads to Eq. (A.9) did not take into account possible correlations between type B components because of the relationship shown in Eq. (A.8). However, calculations of expanded uncertainty, U , using the complete covariance matrix and least-squares fitting using appropriate weights have been carried out and the results are found to be the same as given by Eq. (A.9). The calibration constants in Eq. (A.7) are also found to be about the same as reported.

The blackbody calibration discussed above is for one aperture setting. In general, the point-source blackbodies are equipped with a filter wheel with multiple apertures of various sizes to be able to project different flux levels to the sensor. As the aperture size gets smaller, the uncertainty in its area measurement gets larger. It is possible to measure the effective aperture size

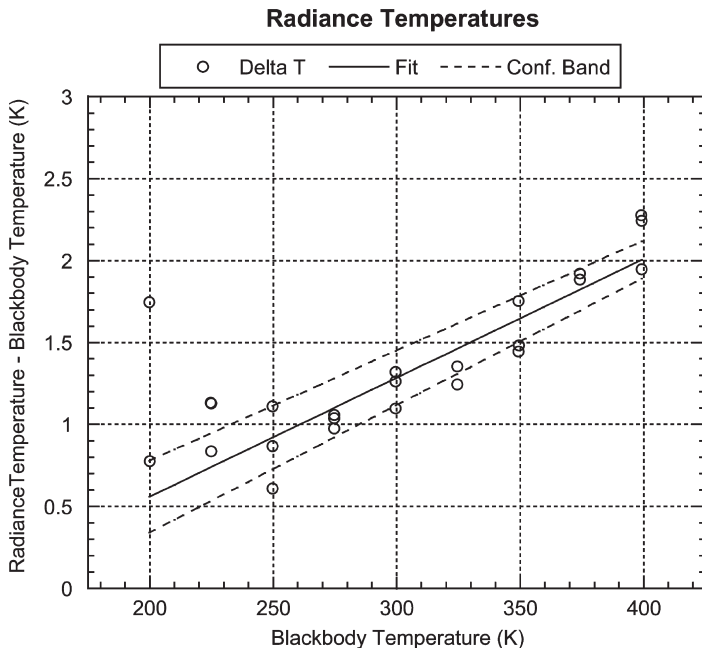


FIG. A.3. The solid line represent difference between the deduced radiance temperature and the temperature measured by the blackbody PRT sensor plotted as a function of the blackbody nominal temperature setting. The circles represent the same for measured radiance temperatures and are not of equal weights. The dashed lines represent upper and lower bounds of 95% confidence bands.

at the cryogenic temperature of operation radiometrically to reduce the aperture measurement uncertainty. Reference [7] discusses this in detail. The method to follow is to determine the radiance of the blackbody core for its highest possible temperature setting and the largest aperture size to ensure that the diffraction correction and aperture area are characterized as well as possible. Under the assumption that the radiance does not change with aperture size, one can deduce the aperture size from the ACR radiant power measurements for other apertures, which probably involves diffraction corrections as well. In this way, the blackbody calibration described here can be carried out for each aperture using radiometrically determined aperture sizes.

A.2.3 Example with Fewer Temperature Settings

In cases where measurements are done at only one or two temperature settings, least-squares analysis as described above is not applicable because of insufficient data. Then the ACR measurement of radiant power at each temperature setting is used to deduce the corresponding radiance temperature using Eq. (A.1). Again, the percentage propagated uncertainty in the deduced radiance temperature is given by Eq. (A.8). The type B components are evaluated as discussed in the previous Section A.2.2. The type A uncertainty in the radiant power measurement is analyzed by pooling the variances between groups of measurements. The radiant power data collected for 3 min leading to approximately 120 data points in each group is averaged to determine the average, \bar{P} , and the standard deviation, s_{rpt} . It is a measure of the repeatability of the measurements in each set, and in general the ACR data show very good repeatability. At least at three different times, the data are taken to have three groups of data to estimate a standard deviation, s_{pr} , for reproducibility. The average power for three runs is calculated as

$$\bar{\bar{P}} = \frac{1}{3} \sum_{j=1}^3 \bar{P}_j \quad (\text{A.10})$$

and a standard deviation, s_t , is calculated from

$$s_t^2 = \frac{1}{2} \sum_{j=1}^3 (\bar{P}_j - \bar{\bar{P}})^2 \quad (\text{A.11})$$

The standard deviation s_t is a measure of both repeatability and reproducibility of the ACR power measurements [1]. The standard deviation of the mean, $s_t/\sqrt{3}$, is the type A uncertainty in the power measurement. In Table A.5, the case for such analysis for measurements at 3 temperature settings are given based on the data of Table A.2. The average power after correcting for diffraction is given in Column 3 and the corresponding uncertainty

TABLE A.5. Analysis of Uncertainty (unc.) in the Case of Fewer Temperature Settings

(1) Nominal blackbody temp. (K)	(2) PRT sensor output (K)	(3) Measured diffraction- corrected power (nW)	(4) Std. dev., s_t (nW)	(5) Radiance temp. (K)	(6) Type A propagated unc. (K)	(7) Type B propagated unc. (K)	(8) Expanded unc., U (K)
300	299.55	361.2	0.4	300.77	0.08	0.38	0.78 (0.3%)
350	349.36	669.8	0.8	350.93	0.10	0.44	0.90 (0.3%)
400	399.07	1144.6	1.3	401.22	0.11	0.50	1.12 (0.3%)

evaluated using Eq. (A.11) is given in Column 4. Column 5 has the radiance temperature, and the propagated type A uncertainty due to uncertainty in radiant power measurement and total propagated type B uncertainty b , obtained as described in Table A.4, are given in Columns 6 and 7. The relative standard uncertainty, $u_{c,r}(T)$, which is the square root of the sum of squares of the propagated uncertainties, is determined. The expanded uncertainty, U , is obtained by multiplying $u_{c,r}(T)$ by the coverage factor 2, which will give less than 95% confidence band because of the small sample size [6]. In any case, the difference between the values predicted in Table A.4 and the deduced temperatures given in Table A.5 are within this expanded uncertainty.

References

1. R. U. Datla, M. C. Croarkin, and A. C. Parr, Cryogenic blackbody calibrations at the National Institute of Standards and Technology low background infrared calibration facility, *J. Res. Natl. Inst. Stand. Technol.* 99, 77 (1994).
2. N. Draper and H. Smith, "Applied Regression Analysis." Wiley, New York, NY, 1981.
3. G. E. P. Box, W. G. Hunter, and J. S. Hunter, "Statistics for Experimenters." Wiley, New York, NY, 1978.
4. J. Neter, W. Wasserman, and M. H. Kutner, "Applied Linear Statistical Models," 2nd edition. Richard Irwin D. Irwin, Inc., Homewood, IL, 1985.
5. M. G. Natrella, "Experimental Statistics." Wiley, NY, 1966.
6. International Organization for Standardization, "Guide to the Expression of Uncertainty in Measurement." Geneva, Switzerland, 1993.
7. A. W. Smith, A. C. Carter, S. R. Lorentz, T. M. Jung, and R. U. Datla, Radiometrically deducing aperture sizes, *Metrologia* 40, S13 (2003).

AUTHOR QUERY FORM

ELSEVIER

Optical Radiometry

JOURNAL TITLE:	EMPS
ARTICLE NO.:	41011

Queries and / or remarks

Query No	Details required	Author's response
	No queries.	